

Petrographically Quantifying the Damage to Field and Lab-cast Mortars Subject to Freeze-thaw Cycles and Deicer Applications

CHUNYU QIAO (✉ joe@drpcinc.com)

DRP, A Twining Company <https://orcid.org/0000-0002-2583-5296>

Nima Hosseinzadeh Nanehkaran

University of Miami

Prannoy Suraneni

University of Miami

Sihang Wei

Bintong Engineering

David Rothstein

DRP, A Twining Company

Research Article

Keywords: Concrete petrography, substrate mortar, calcium oxochloride, freeze-thaw cycles, deicers

Posted Date: March 5th, 2021

DOI: <https://doi.org/10.21203/rs.3.rs-271595/v1>

License:   This work is licensed under a Creative Commons Attribution 4.0 International License.

[Read Full License](#)

Version of Record: A version of this preprint was published at Journal of Infrastructure Preservation and Resilience on April 14th, 2021. See the published version at <https://doi.org/10.1186/s43065-021-00024-3>.

1 Petrographically quantifying the damage to field and lab-cast mortars subject to freeze-thaw
2 cycles and deicer applications

3 Chunyu Qiao^{a*}, Nima Hosseinzadeh Nanehkaran^b, Prannoy Suraneni^b, Sihang Wei^c and David Rothstein^a

4 a. *DRP, A Twining Company, Boulder, CO 80301, USA*

5 b. *Department of Civil, Architectural and Environmental Engineering, University of Miami, Coral
6 Gables, FL 33146, USA*

7 c. *Bintong Engineering, Shenzhen, Guangdong 518052, China*

8 * Corresponding author: Chunyu Qiao, Email: joe@drpcinc.com

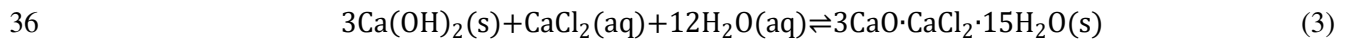
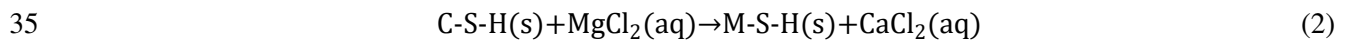
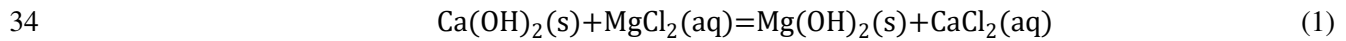
9 **ABSTRACT**

10 Although calcium oxychloride (Ca-Oxy) is known to damage cementitious materials exposed to calcium
11 chloride (CaCl₂) deicers, there is little direct observation of Ca-Oxy in the field due to its instability. This
12 paper uses optical microscopy (OM) and scanning electron microscopy coupled with energy dispersive X-
13 ray spectrometry (SEM-EDX) to detect the formed Ca-Oxy and quantify its associated damage in a field
14 mortar subject to freeze-thaw cycles and deicer applications. The characterized damage in the field mortar
15 is compared to that in lab-cast portland cement paste and mortar which are submerged in a CaCl₂ solution
16 of 25 wt. % under freeze-thaw cycles (-8 to 25 °C). The field and lab-cast mortars show similar cracking
17 patterns that are parallel to the exposure surface with a variation of 30-45° in the preferred orientation due
18 to the constraints of sand particles. During each lab-controlled freeze-thaw cycle, the high CaCl₂
19 concentration of 25 wt. % stabilizes the formed Ca-Oxy, which continually damages the mortar and
20 eventually results in 3-4 times higher crack density compared to that in the field mortar. SEM-EDX analysis
21 confirms the presence of secondary deposits including Friedel's salt, ettringite and Ca-Oxy. Image analysis
22 on thin section photomicrographs shows a reduction of 86.4% in calcium hydroxide (Ca(OH)₂) content in
23 the damaged field mortar compared to the undamaged field mortar, suggesting significant leaching of
24 Ca(OH)₂ to form Ca-Oxy due to the deicer application.

25 **Keywords:** Concrete petrography; substrate mortar; calcium oxychloride; freeze-thaw cycles; deicers.

26 **1. Introduction**

27 Chloride-based inorganic salts, such as sodium chloride (NaCl), magnesium chloride (MgCl₂) and calcium
28 chloride (CaCl₂), are the most commonly used deicing agents on concrete pavements in cold regions for
29 melting snow and ice [1-4]. However, chloride ions from deicing salts can infiltrate or diffuse into the
30 concrete, which accelerates the corrosion of the steel reinforcement and diminish the service life of concrete
31 pavements [5,6]. MgCl₂ and CaCl₂ can also react with hydration products to form secondary phases such
32 as brucite (Mg(OH)₂), magnesium-silicate hydrate (M-S-H) and calcium oxychloride (Ca-Oxy), that can
33 damage cementitious materials through multiple reactions [7,8]:



37 The reactions associated with MgCl₂ in Eq. 1 and 2 generally occur at the exposure surface since the
38 formation of insoluble brucite blocks the pathway for further ingress [9,10,7]. The pore-blocking
39 phenomenon leads to substantially lower chloride penetration depth in concrete exposed to MgCl₂ solutions
40 compared to that exposed to NaCl solutions [11].

41 The formation of Ca-Oxy shown in Eq. 3 is expansive [12], which builds up internal stress to cause damage
42 from cracking and microcracking [8]. Pioneering research on the damage to concrete due of Ca-Oxy
43 formation dates back to the 1970s [12], and this topic was discussed in some detail in two recent review
44 papers [13,14]. However, very few studies have clearly shown Ca-Oxy crystals formed in field concrete;
45 this is likely due to its thermodynamic instability and its tendency to break down during the carbonation
46 process [15]. The Ca(OH)₂-CaCl₂-H₂O phase diagram illustrates the reversible nature of Ca-Oxy formation
47 [12,16]. Because Ca-Oxy is prone to decompose as the ambient temperature increases, it is extremely
48 difficult to preserve Ca-Oxy in cores or other samples of field concrete after winter or after they are removed
49 from cold environments. Peterson et al. [15] hypothesized a decomposition path from Ca-Oxy to calcite to
50 explain the lack of convincing field evidence of Ca-Oxy associated damage in pavements exposed to
51 significant deicers.

52 In this work, we provide further insights into Ca-Oxy associated damage in field and lab specimens using
53 microscopic methods. As a concrete petrography method, fluorescence microscopy (FM) has been
54 implemented to quantify damage over the last three decades [17,18]. Reliable crack quantification by FM
55 depends heavily on two aspects: (a) the fluorescent dye should be uniformly and thoroughly introduced and
56 dispersed along all cracks and microcracks; and (b) the fluorescent dye should be only retained in cracks
57 and microcracks on the examined surface [18]. The first aspect is realized by proper impregnation of
58 fluorescent dye in resin or organic solute such as ethanol [17]. The second aspect is assured by proper
59 polishing after impregnation [18]. Multiple algorithms and tools have been applied for quantitative crack
60 analysis after obtaining the images [18-20], however, little research has focused on performing crack
61 detection and quantification using well-developed tools such as ImageJ that have been widely used for
62 biological and medical research [21].

63 In addition to contrast enhancement for crack detection, FM shows the potential to illustrate the capillary
64 porosity in the cement paste matrix of concrete [22,23]. One important application is to determine water to
65 cement ratio (w/c) [23]. More generally, the sensitivity of fluorescent light intensity on capillary porosity
66 makes it an indicator of the microstructural alteration along the depth in cementitious materials subject to
67 chemical attacks such as microbially induced corrosion [24].

68 Optical microscopy (OM) and scanning electron microscopy (SEM) are also powerful tools to discover
69 changes in chemistry and mineralogy when cementitious materials are exposed to chemically deleterious
70 environments [22]. For instance, OM and SEM have been commonly used to diagnose alkali-silica reaction
71 in concrete, and characterize the mineral component of reactive aggregate and the chemical composition of
72 ASR gel [25,26].

73 This paper uses OM and FM to detect cracking and microstructural mineralogical alteration in field and
74 lab-cast cementitious mortars due to freeze-thaw cycles and deicer application. ImageJ is used to quantify
75 cracks/microcracks in the field mortar and compare cracking to that in the lab-cast mortar and paste. SEM
76 coupled with energy dispersive X-ray spectrometry (SEM-EDX) is used to characterize the morphology of
77 secondary deposits and analyze their elemental compositions in the damaged field and lab-cast mortars.

78 Image analysis is also performed on photomicrographs of thin sections to quantitatively investigate the
79 leaching of $\text{Ca}(\text{OH})_2$ due to deicer application.

80 **2. Materials and experimental methods**

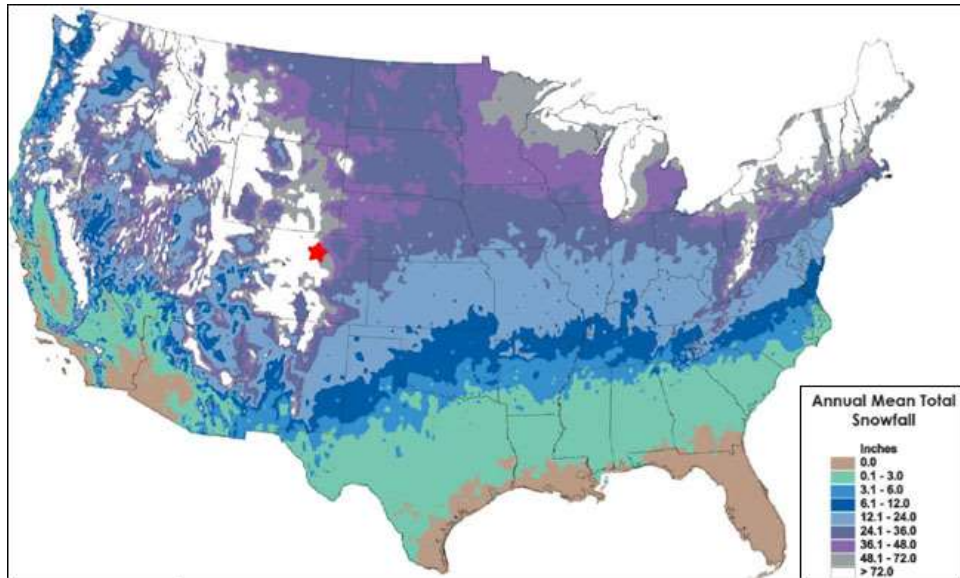
81 **2.1 Materials**

82 *2.1.1 Field mortars*

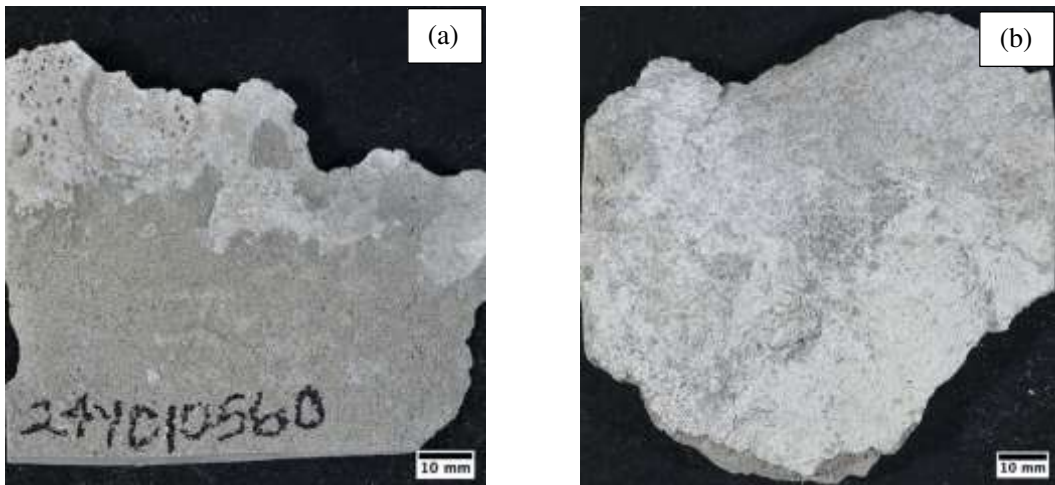
83 The studied field mortar samples were obtained from substrate slabs that were designed to support tactile
84 warning tiles at a public transit facility in the Rocky Mountain Region of the US. The substrate slabs were
85 placed in 2014 and samples were obtained in 2020 after the slabs had been in service for six winter seasons.

86 Fig. 1 shows the average annual snowfall accumulation in the contiguous US (US National Oceanic and
87 Atmospheric Administration: <https://www.noaa.gov>). The average annual snowfall in the region where the
88 samples are from is in the range of 122-182 cm, and the exterior slabs were subject to frequent freeze-thaw
89 cycles in winter. A deicer primarily consisting of CaCl_2 was reportedly used in the first two winter seasons,
90 while a deicer primarily consisting of MgCl_2 was reportedly used in the following four winter seasons.

91 Two mortar samples designated as “undamaged field mortar” and “damaged field mortar” are shown in Fig.
92 2. The hard and compact undamaged field mortar was obtained from a relatively dry sheltered corner that
93 did not see significant deicer application. The friable damaged field mortar was obtained from a wet
94 unsheltered zone with significant deicer exposure. Both samples were fragmented during sampling. The
95 damaged field mortar shows white secondary deposits on the fragment surface. Although the exact mixture
96 design remains unknown, petrographic examinations indicate that the mortar samples are non-air-entrained
97 and do not contain any supplementary cementitious materials (SCMs). The damaged field mortar has had
98 long-term contact with deicer solutions through the edge of the tiles, considering the top surface of the
99 substrate slab is lower than the surrounding platform.



100
 101 **Fig. 1** Average annual snowfall map of the contiguous US from US National Oceanic and Atmospheric
 102 Administration (<https://www.noaa.gov>). The red star indicates the location of the field samples.
 103



104
 105 **Fig. 2** The conditions of the as-received fragments of the undamaged field mortar (a) and the damaged
 106 field mortar (b), respectively.
 107

108 *2.2.2 Lab-cast cement paste and mortar*

109 Type I/II OPC was used to prepare an OPC paste and mortar in the lab for the comparative study with the
 110 field mortar. The fine aggregate was a siliceous sand with a nominal maximum size of 4.75 mm and an
 111 absorption of 2.84%. Aggregates were corrected for water content before mixing. The OPC paste (P1) and

112 mortar (M1) were mixed using a water-to-cement ratio (w/c) of 0.40; the mortar had a sand-to-cement ratio
113 of 2.0. The mixtures P1 and M1 were mixed using a benchtop mixer following ASTM C305, cast into 50-
114 mm cubes and then cured in a moist room at 23 °C for 28 days.

115 *2.2.3 CaCl₂ solution*

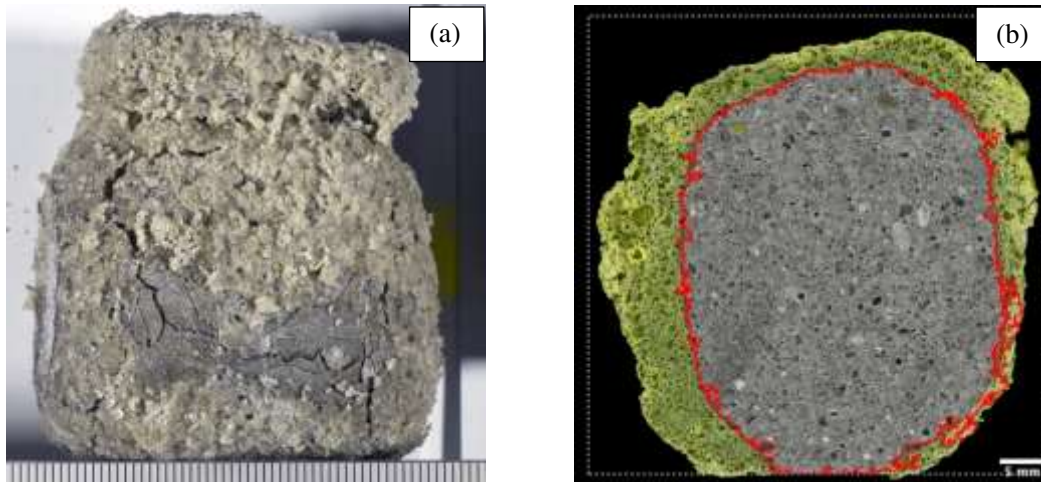
116 Since the damage induced by MgCl₂ is limited to a shallow zone next to the exposure surface [7], the lab-
117 cast P1 and M1 were only exposed to a CaCl₂ solution during freeze-thaw cycles to mimic the damage by
118 CaCl₂ in the field. A commercial deicer CaCl₂ with a purity >95 wt. % was used to prepare solutions with
119 a CaCl₂ concentration of 25 wt. % by mixing the salt with tap water in the appropriate weight proportions.

120 **2.2 Experimental methods**

121 *2.2.1 Freeze-thaw cycles*

122 At the age of 28 days, P1 and M1 were submerged in 25 wt. % CaCl₂ solutions (liquid/solid ratio 0.7) in a
123 sealed container and then moved into a freezer for 24 hours. Temperature was monitored in areas around
124 the specimens during the 24-hour period; the recorded minimal temperature was -8 ± 1 °C, which is
125 comparable to the average low temperature at the studied field location during the winter. After 24 hours
126 in the freezer, the container was removed from the freezer and kept under ambient conditions (25 ± 1 °C)
127 for 24 hours, after which the procedure was repeated. Thus, each freeze-thaw cycle lasted 48 hours.
128 Although the ambient temperature was below 0 °C for 24 hours during each freezing stage, the specimen
129 temperature remained below 0 °C for only about 7 hours. Considering the high CaCl₂ concentration of the
130 submersion solution, it is unlikely that actual freezing occurred.

131 Fine cracks (minor damage) were initially detected on the edges of P1 cubes after eight freeze-thaw cycles
132 and the specimen disintegrated completely after 51 cycles (failure). Fine cracks were observed in M1 after
133 seven cycles; M1 became friable and exhibited signs of severe damage (significant spalling and swelling)
134 after 53 cycles and disintegrated completely after 142 cycles (failure). Specimens were collected for
135 petrographic examinations after disintegration (51 cycles for P1 and 142 cycles for M1).



136
137 **Fig. 3** (a) Photograph showing condition of the lab-cast mortar after 51 freeze-thaw cycles under the
138 submersion of a 25 wt. % CaCl_2 solution. Scale in millimeters. (b) Reflected light photomicrograph of the
139 polished surface of the lab-cast mortar. White square and red curve indicate the original size and the
140 remaining intact zone of the sample, respectively. The yellow green color in (b) indicates the epoxied
141 damage zone.

142 2.2.2 *Optical microscopy (OM)*

143 Optical microscopy was conducted on a polished slab and a thin section that represents a longitudinal cross
144 section of each mortar sample (two field mortars and one lab-cast mortar) according to ASTM C856-20
145 [27]. Epoxy that contains fluorescent dye was used to stabilize the damaged field and lab-cast mortars prior
146 to the polished slab preparation. Thin sections of all samples were impregnated with an epoxy containing
147 fluorescent dye and ground and polished to a thickness of 20-25 μm by an automatic thin section machine
148 (PELCON). A stereomicroscope (NikonTM SMZ-25) and a petrographic microscope (NikonTM E-Pol 600)
149 were used to examine the polished slabs and thin sections, respectively.

150 2.2.3 *Scanning electron microscopy coupled with energy dispersive X-ray spectrometry (SEM-EDX)*

151 A scanning electron microscope (FEITM Quanta 250) coupled with an energy dispersive X-ray (EDX,
152 Thermo ScientificTM UltraDry EDS) was used to examine the morphology and elemental compositions of
153 secondary deposits that line cracks, microcracks and voids in the samples. Uncoated fracture surfaces of
154 each sample were examined in the low vacuum (~ 70 Pa) mode using an accelerating voltage of 15 kV at a
155 working distance of 10 mm.

156 3. Damage quantification

157 Fig. 4 shows the cracking patterns in the damaged field mortar, lab-cast mortar and paste after exposure to
158 freeze-thaw cycles and deicers. Each sample exhibits a network of interconnected cracks (0.1-1 mm in
159 width) and microcracks (< 0.1 mm in width). The cracks and microcracks are subparallel to the exposure
160 surface and cut around aggregate particles, which consist mostly of quartz grains. Without the restraint
161 imposed by fine aggregate particles, the cracks in the lab-cast paste P1 are parallel to each other, and each
162 delamination sheet in P1 has approximately the same thickness of $200 \pm 25 \mu\text{m}$. These characteristics are
163 typical of damaged observed from freeze-thaw cycles [22].

164 Secondary deposits were observed to fill cracks and microcracks near the exposed surface in each sample,
165 as shown in Fig. 4a, 4c and 4f. This is consistent with the formation of Ca-Oxy due to the application of
166 CaCl_2 [15]. The secondary deposits are white and translucent on the polished surface of two mortars (in
167 Fig. 4a and 4c), while they are transparent on the fresh surface of the delamination sheet in the paste (in
168 Fig. 4f). The difference in appearance is likely related to drying effects during the preparation of the
169 polished surface [15].

170 Fig. 5a-5d show bright green cracks/microcracks that are filled with epoxy containing fluorescent dye under
171 the ultraviolet light. Since very little epoxy is able to penetrate the paste from the cracks/microcracks, the
172 paste matrix and aggregate are dark green to black as background. This enhanced contrast between the
173 cracks/microcracks and matrix affords an opportunity to quantify cracking through image analysis. Cracks
174 and microcracks can be automatically recognized and extracted on the polished surfaces using a plugin
175 “Ridge Detection” in ImageJ [28], as illustrated in Fig. 5e-5h. The “Ridge Detection” plugin requires three
176 parameters: (a) line width; (b) highest grayscale value of the line; and (c) lowest grayscale value of the line.
177 After several trials, the values of the three parameters were determined as 15 pixels, 255 and 80, respectively,
178 for the best detection. The above process output three important parameters regarding the cracking
179 characteristics, i.e., the length, mean width and orientation of each crack/microcrack.

180 As geometric features of a partially connected crack network, the orientations of cracks/microcracks are
181 closely related to the fracture process and progress in solids [20]. Fig 5i-5l show rose diagrams of

182 crack/microcrack orientations at different depths in the damaged field and lab-cast mortars. The statistical
183 data of cracking orientations further confirms the preferred cracking direction that tends to be parallel to
184 the exposure surface of both field and lab-cast mortars. There is a variation of 30-45° in the preferred
185 orientation due to the constraints of sand particles in the mortar.

186 Cracking length and mean width are direct measures of the extent of material damage. They are used to
187 calculate crack density (l , mm/mm²) and crack area fraction (s , unitless) as follows:

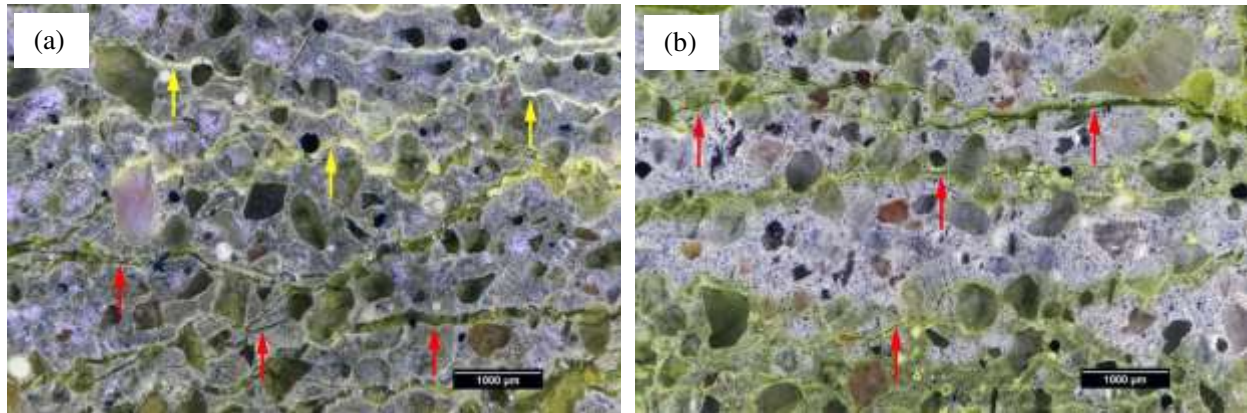
$$188 \quad l = \frac{\sum L_{crack}}{SS} \quad (4)$$

$$189 \quad s = \frac{\sum L_{crack} \cdot W_{crack}}{SS} \quad (5)$$

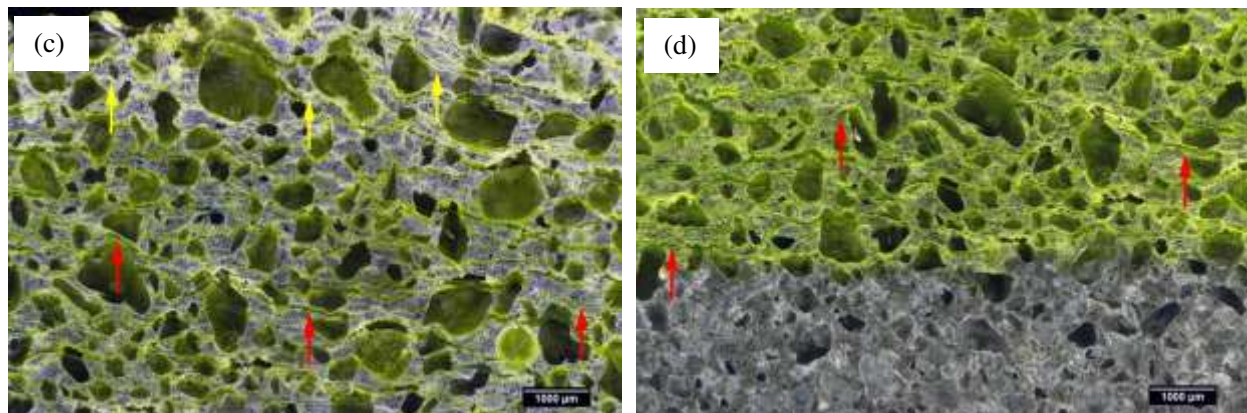
190 where, L_{crack} (mm) and W_{crack} (mm²) are the length and mean width of a crack/microcrack in the selected
191 zone with an area of SS (mm²). Although somewhat differing definitions of crack density have been adopted
192 in previous studies [18,20], this paper uses Eq. 4 to define the crack density for the following discussion.

193 Fig. 6 summarizes the measured results in randomly selected zones (Fig. 5) at two different depths of each
194 damaged mortar. In both damaged mortars, the area further from the exposure surface shows a lower crack
195 density and area fraction, which indicates the progression of damage with depth. It is impossible to obtain
196 the absolute depth of the selected zones since the original exposure surface had been missing due to severe
197 damage. Compared to the damaged field mortar, the lab-cast mortar shows approximately 3-4 times higher
198 crack density and 1-3 times higher crack area percentage, indicating more damage occurred under the
199 accelerated exposure conditions realized in the laboratory. The phase diagram for the Ca(OH)₂-CaCl₂-H₂O
200 system demonstrates that Ca-Oxy is a stable phase in a 25 wt. % CaCl₂ solution at a temperature lower than
201 40 °C [29]. This implies that the formed Ca-Oxy was able to constantly damage the lab-cast mortar
202 throughout each freeze-thaw cycle (-8 °C to 25 °C). In the field, external factors, such as loss of the deicer
203 solutions from drainage and dilution of these solutions from rainfall, reduce the potential for Ca-Oxy to be
204 a stable phase. Additional Ca-Oxy destabilization also occurs from carbonation, which is minimized in the
205 lab due to constant submersion in the deicer solution. [15].

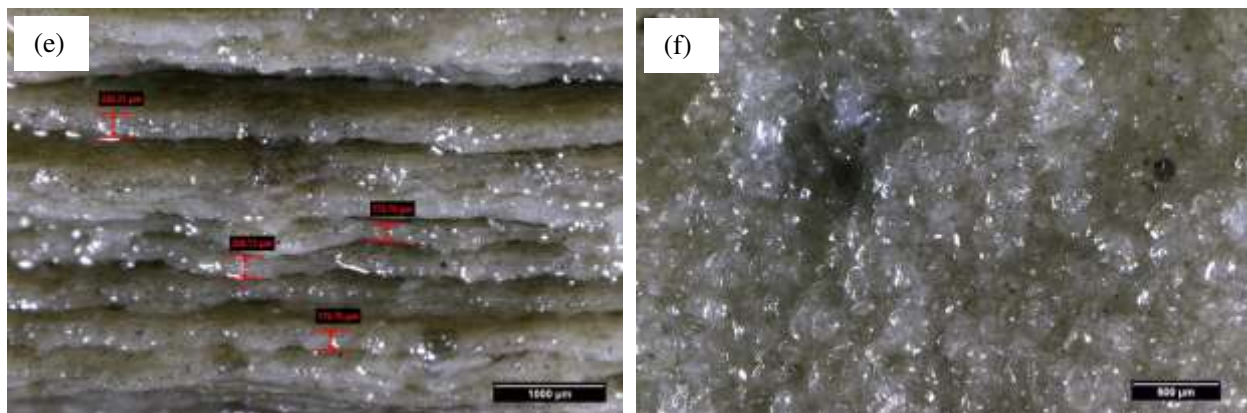
206



207

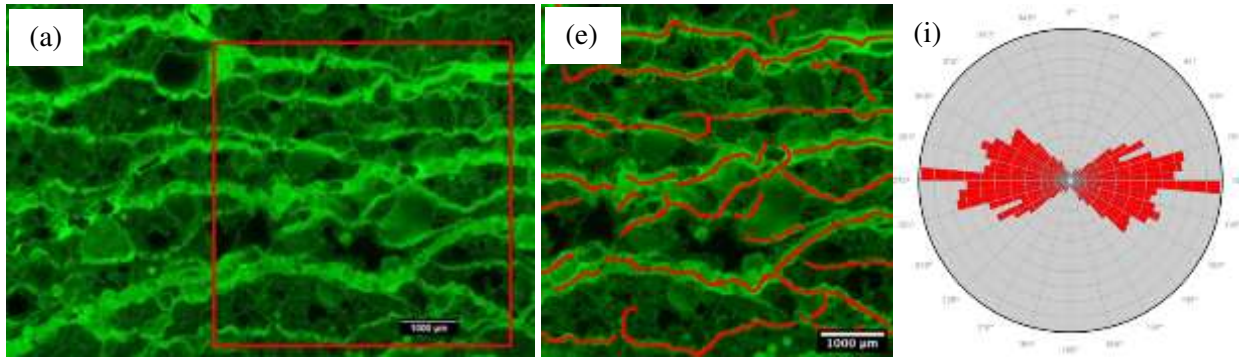


208

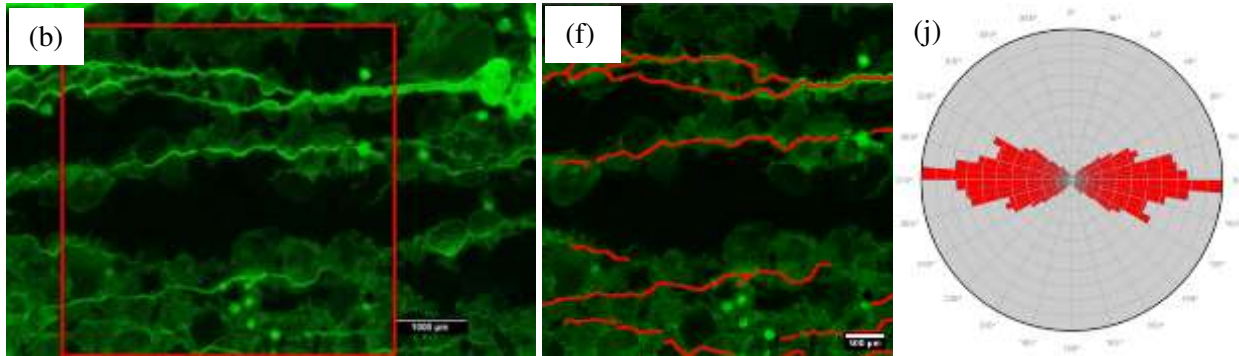


209 **Fig. 4** (a)-(d) Reflected light photomicrographs (RLP) of the polished surface of the damaged field mortar
210 (a-b) and lab-cast mortar (c-d) showing horizontal cracks/microcracks at two different depths from the
211 exposure surface, respectively. Zones in (a) and (c) are closer to the exposure surface. Yellow and red
212 arrows indicate cracks/microcracks with and without secondary deposits, respectively. (e) Fresh
213 delamination sheets in the damaged lab-cast paste. (f) Transparent secondary deposits on the surface of
214 the delamination sheet in (e).

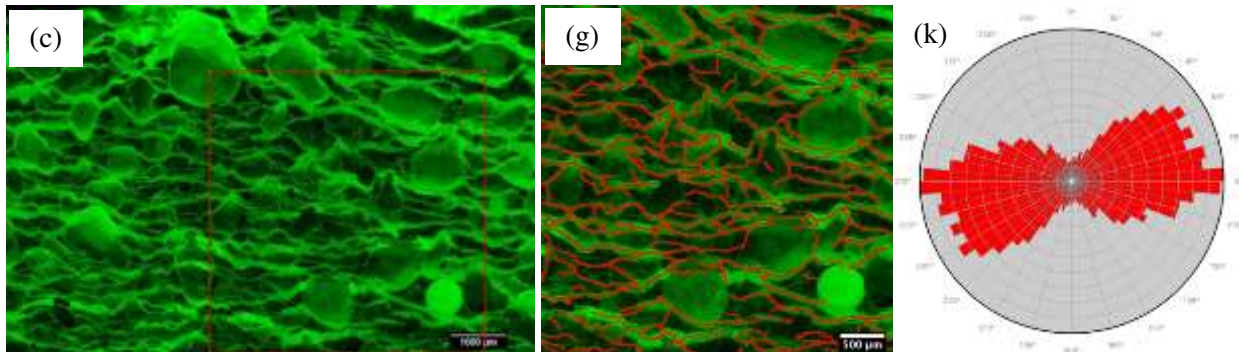
215



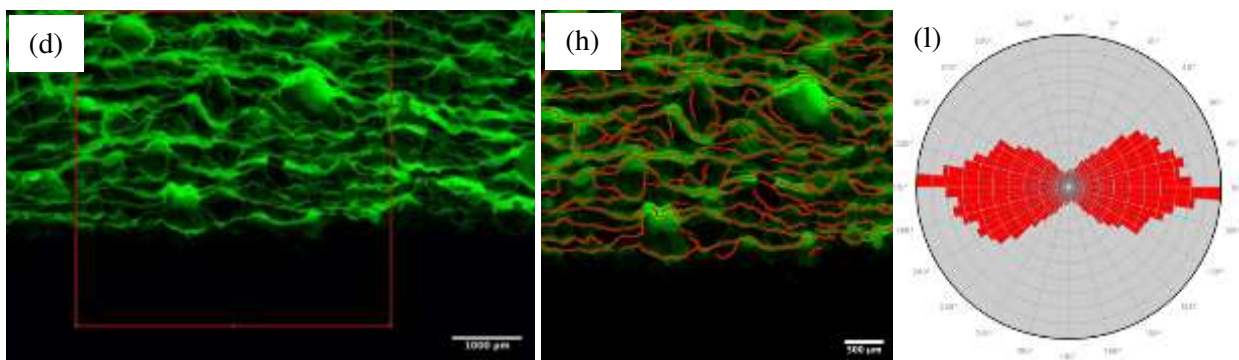
216



217



218



219

220

221

222

223

Fig. 5 (a)-(b) Fluorescent reflected light photomicrographs (FRLP) of the polished surface of the damaged field mortar showing cracks/microcracks in the upper and lower zones from the top surface, respectively. (c)-(d) FRLP of the polished surface of the lab-cast mortar showing cracks/microcracks in the closer (outward) and further (inward) zones from the outer surface, respectively. (e)-(h) Identified crack network in the red zone in (a)-(d). (i)-(l) Rose diagrams showing the cracking orientation in (e)-(h).

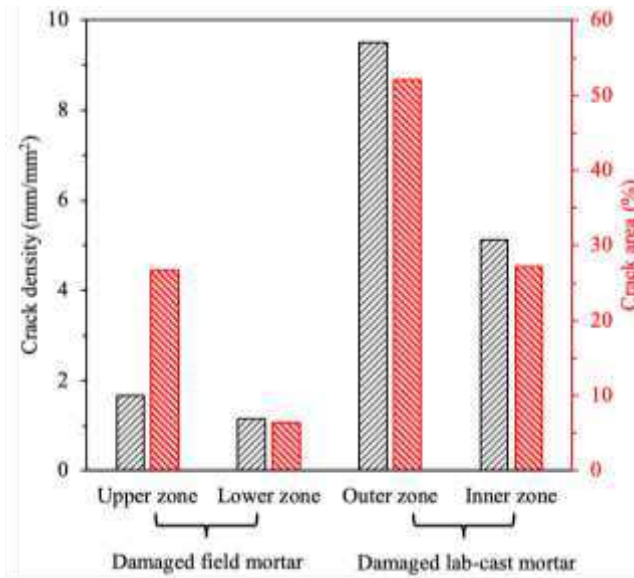


Fig. 6 Crack density (left series) and crack area fraction (right series) in different zones of the field damaged field mortar and lab-cast mortar.

4. Mineralogical alteration quantification

4.1 Secondary deposits

SEM-EDX was used to examine the secondary deposits observed in the damaged field mortar and lab-cast paste after exposure to CaCl_2 deicer solutions. To avoid the chemical and physical alteration of secondary deposits during sample preparation, only fresh fracture surfaces of each sample were examined. Fig. 7 shows the morphology of secondary deposits in different locations of the damaged field mortar. Although a well-polished surface renders EDX semi-quantitative analyses at best, one can still recognize the elemental composition of phases of interest on fracture surfaces. Multiple secondary deposits were observed in the damaged field mortar as follows:

(a) *Friedel's salt*. As the external chloride ions penetrate the cement-based mortar, they react with calcium monosulfoaluminate (AFm) and its iron analog to form Friedel's salt [30], which is distributed in the paste matrix in Fig. 7a.

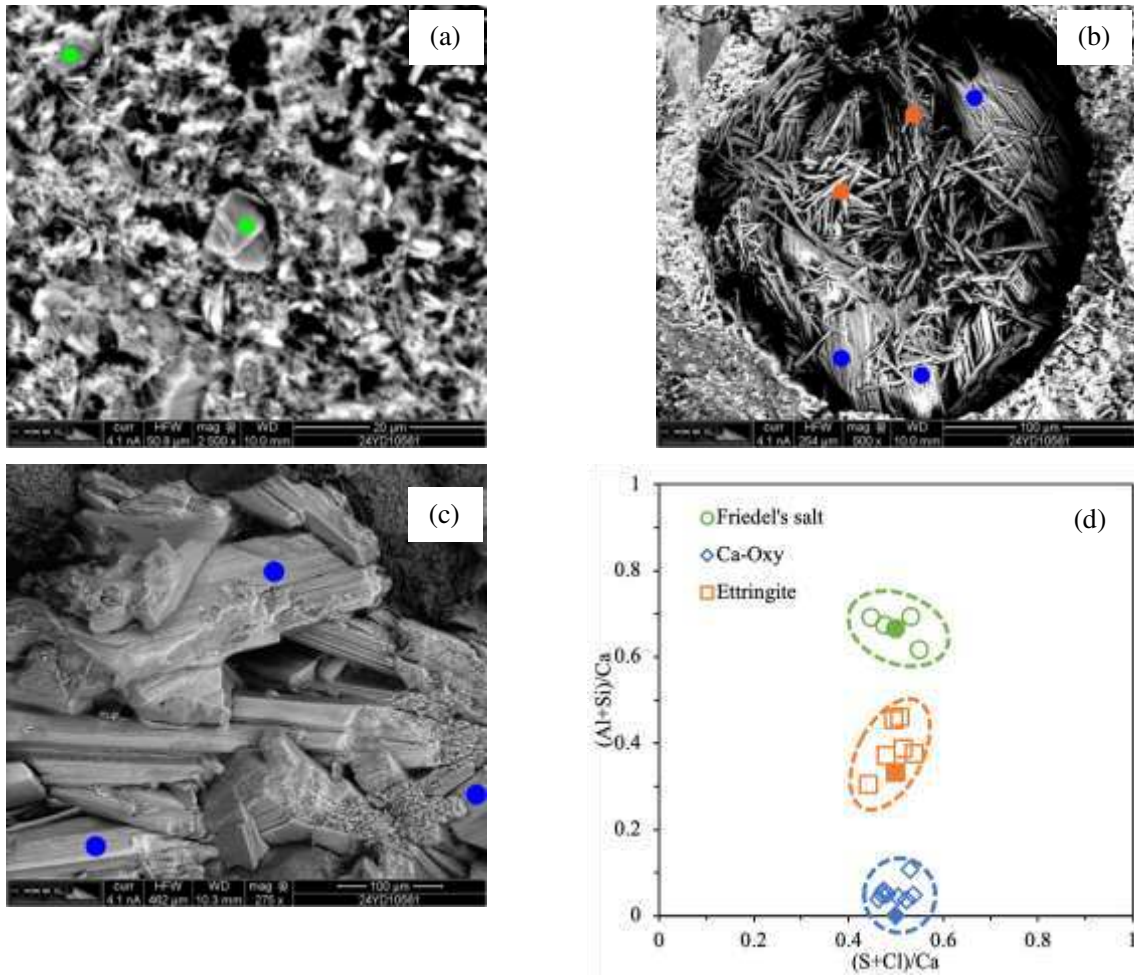
(b) *Ettringite*. Clusters of fibrous secondary ettringite were observed filling air voids, as shown in Fig. 7b. The conversion of AFm to Friedel's salt by ionic exchange releases sulfate ions, which can further react with the remaining AFm to form secondary ettringite [31,32]. The presence of external

243 deicers in the pore solution leads to a relatively high internal humidity in the mortar, and this helps
244 stabilize ettringite that has a high water content (32 H₂O molecules) [33].

245 (c) *Ca-Oxy*. *Ca-Oxy* forms when CaCl₂ deicer reacts with Ca(OH)₂ in the cement paste (Eq. 3). *Ca-*
246 *Oxy* manifests as prismatic crystals that were observed filling air voids and lining
247 cracks/microcracks in Fig. 7b-7c. This is consistent with previous observations by Galan et al. [34].
248 The *Ca-Oxy* crystals exhibit a series of developed microcracks parallel to the prism axis, which
249 may be related to partial dehydration of the crystals in the SEM vacuum chamber [34].

250 The observed secondary deposits were chemically analyzed and verified using EDX in Fig. 7d, which shows
251 that they have comparable elemental ratios to the corresponding theoretical formulas. No evidence of
252 significant deposits of brucite or M-S-H was observed within in the damaged field mortar. This is consistent
253 with brucite blocking pores at the exposure surface [11,7].

254 The sensitivity of *Ca-Oxy* morphology to drying is further investigated in the lab-cast paste P1. Fig. 8 shows
255 the different *Ca-Oxy* crystals that are freshly obtained from P1 and vacuum dried in the SEM chamber at a
256 vacuum level of ~ 70 Pa for 12 hours. Compared to the fresh *Ca-Oxy* crystals, the dried *Ca-Oxy* crystals
257 become white and translucent to opaque (Fig. 8a-8b), which is related to the white secondary deposits filling
258 cracks/microcracks on the polished surfaces of mortars in Fig. 4a and 4c. Moreover, the dried *Ca-Oxy*
259 prisms shrank and further cracked due to the loss of water, as shown in Fig. 8c-8d. This is consistent with
260 previously reported observations [34]. EDX analysis in Fig. 8e-8f shows that the majority of dried *Ca-Oxy*
261 crystals maintain the same elemental composition as the fresh *Ca-Oxy* crystals. However, a portion of dried
262 *Ca-Oxy* crystals may have been converted to a type of calcium oxychloride without water, e.g.
263 Ca(OH)₂-CaCl₂, as shown in Fig. 8f.

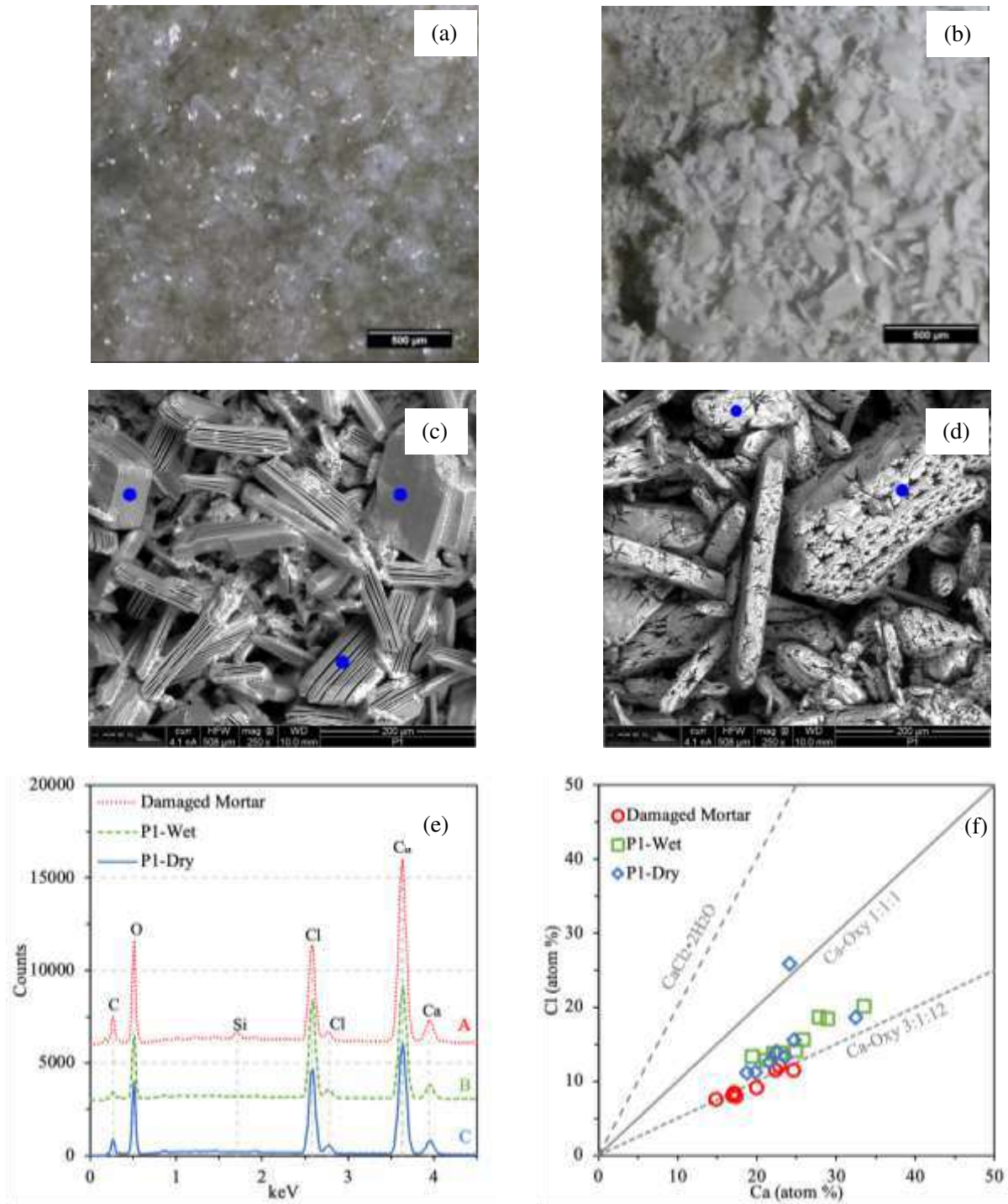


264 **Fig. 7** (a)-(c) Backscattered electron (BSE) images of secondary deposits in (a) the paste matrix, (b) an
 265 entrained air void and (c) a fresh fracture surface, respectively. Green circles: Friedel's salt, blue
 266 diamonds: Ca-Oxy; orange squares: ettringite. (d) Atomic ratios obtained from EDX spectra in zones in
 267 (a)-(c). The solid shapes indicate the theoretical composition of the corresponding minerals.

268

269

270



271 **Fig. 8** (a)-(b) RLP and (c)-(d) BSE images of Ca-Oxy (blue solid dots) in (a)/(c) an originally wet
 272 condition and (b)/(d) a dried condition on a fracture surface of OPC paste, respectively. (e) EDX spectra
 273 obtained from zones in Fig. 5c and Fig. 6a-6b. (f) Relationship between Ca and Cl contents of Ca-Oxy
 274 observed from EDX overlaid with theoretical Ca-Oxy formulae.
 275

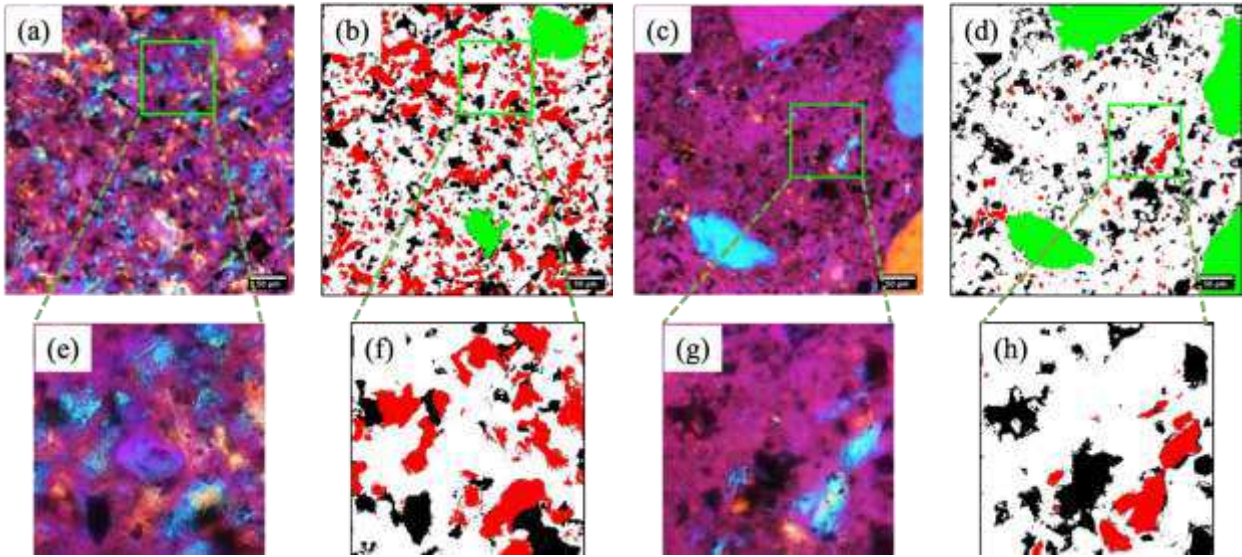
276 4.2 Ca(OH)₂ leaching

277 Fig. 9 highlights Ca(OH)₂ present in the undamaged and damaged field mortars via transmitted cross-
278 polarized light microscopy with the first order retardation plate. The Ca(OH)₂ crystals are in first order
279 yellow and second order blue interference colors. The undamaged field mortar shows Ca(OH)₂ crystals
280 evenly distributed in the paste matrix, while Ca(OH)₂ crystals are scarce in the damaged field mortar paste.
281 This finding directly confirms that the deicer application, especially CaCl₂, can lead to the leaching of
282 Ca(OH)₂ in the field due the formation of Ca-Oxy [32,7]. MgCl₂ deicer can also consume Ca(OH)₂ due to
283 the formation of brucite, but its influence is limited in areas adjacent to the exposure surface considering
284 the absence of brucite in the bulk of the examined samples.

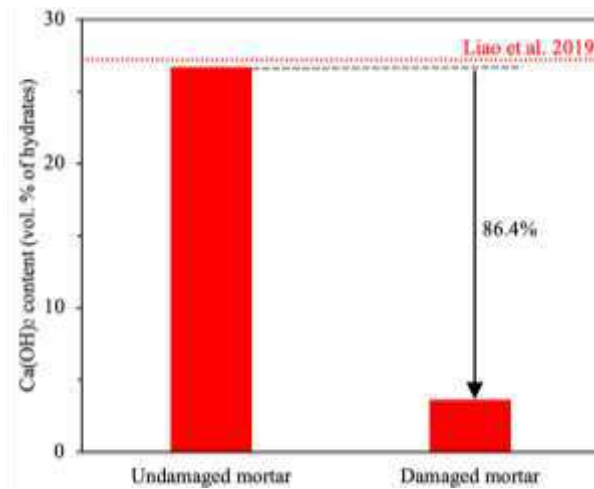
285 Since Ca(OH)₂ crystals show distinct colors from the other hydrates in the paste matrix in Fig. 9a and 9c,
286 image segmentation can be performed to quantify the volume (area) fraction of Ca(OH)₂ crystals in the
287 paste matrix. Firstly, the aggregate particles were selected and excluded (green areas in Fig. 9b and 9d)
288 manually in ImageJ before the segmentation. The remaining section in each image truly represents the paste
289 matrix. Three classes of components are categorized as follows: (a) Ca(OH)₂ crystals that are in in first
290 order yellow and second order blue interference color; (b) the other hydrates that are in purple as
291 background; and (c) the unhydrated cement particles that are opaque in dark brown to black. The image
292 segmentation were performed using the plugin “Trainable Weka Segmentation” in ImageJ [35]. This plugin
293 provides pixel-based segmentation using multiple machine learning algorithms together with a set of
294 selected image features. Three classes of pixels were defined based on the above three components in the
295 paste. After different areas were selected and assigned to each class as inputs, the plugin automatically
296 produces satisfactory segmentation after a few training instances, as shown in Fig. 9b and 9d. The zoomed
297 in areas in Fig. 9e-9h indicate that the machine learning based segmented areas agree well with the actual
298 corresponding components.

299 Fig. 10 plots the volumetric (area) fraction of Ca(OH)₂ normalized to the total hydrates in the paste.
300 Compared to the undamaged field mortar, the damaged field mortar shows a significant reduction of 86.4%
301 in Ca(OH)₂ based on the above image analysis. The analyzed Ca(OH)₂ volumetric faction (26.7%) in the

302 hydrates of the undamaged field mortar is similar to that of 27.2% reported by Liao et al. [36]. This shows
 303 the reliability and feasibility of applying optical microscopy coupled with image analysis to quantitatively
 304 investigate the chemical alteration caused by deicers. This methodology can be further extended to analyze
 305 other durability-related microstructural alteration if a distinct feature can be defined under microscopes.



306
 307 **Fig. 9** (a)&(c) Transmitted light photomicrographs showing paste in the middle of the (a) undamaged
 308 field mortar and (c) damaged field mortar, respectively, in cross-polarized light with the gypsum first
 309 order retardation plate inserted. (b)&(d) Segmentation images of the photomicrographs in (a) and (c)
 310 using 2D Trainable Weka Segmentation in ImageJ [35]. (e)-(h) Zoomed-in images of the corresponding
 311 zones in (a)-(d). The size of the zone in (e)-(h) is 100 μm by 100 μm.



312
 313 **Fig. 10** Quantification of Ca(OH)₂ contents in the mortars using image analysis. The red dotted line
 314 indicates the value from Ref. [36].

315 **5. Conclusions**

316 This paper demonstrates the utility of combining petrographic methods with image analysis to quantify
317 damage of cementitious materials exposed to freeze-thaw cycles and chloride-based deicers. The damaged
318 field and lab-cast mortars show similar cracking patterns including: (a) a network of interconnected
319 cracks/microcracks that are parallel to the exposure surface; and (b) lowered crack density over the depth.
320 Both damaged field and lab-cast mortars show a variation of 30-45° in the preferred orientation due to the
321 constraints of sand particles. Compared to the damaged field mortar, the lab-cast mortar shows 3-4 times
322 higher crack density and 1-3 times higher crack area fraction because the accelerated lab exposure
323 conditions are far more severe than the field exposure conditions.

324 SEM-EDX analysis confirms the elemental compositions of three distinct secondary deposits: Friedel's salt,
325 ettringite and Ca-Oxy. The altered appearance of Ca-Oxy after drying demonstrates the influence of sample
326 preparation on the formed Ca-Oxy.

327 Transmitted cross-polarized light microscopy with the first order retardation plate can be used to perform
328 image segmentation and quantify the volume fraction of Ca(OH)₂ in the cement-based materials. Compared
329 to the undamaged field mortar, the damaged field mortar shows a reduction of 86.4% in Ca(OH)₂ content,
330 suggesting the significant leaching of Ca(OH)₂ due to the formation of Ca-Oxy.

331

332 **Acknowledgements**

333 The authors gratefully thank the assistance of Mr. Gaines Green and Ms. Grace Guryan for sample
334 preparation at DRP, A Twining Company.

335

336 **Authors' contribution**

337 Chunyu Qiao: Conceptualization, Methodology, Investigation, Formal analysis, Resources, Writing
338 Original Draft, Supervision, Project administration.

339 Nima Hosseinzadeh Nanekaran: Investigation, Resources, Review & Editing.

340 Prannoy Suraneni: Investigation, Resources, Review & Editing, Funding acquisition.

341 Sihang Wei: Investigation, Review & Editing.

342 David Rothstein: Investigation, Project administration, Review & Editing.

343

344 **Funding**

345 Funding assistance from Ready Mixed Concrete Research and Education Foundation for the project “The
346 role of air content and supplementary cementitious materials replacement in deicing salt joint damage in
347 concrete” is acknowledged.

348

349 **Availability of data and materials**

350 Some or all data generated or used during the study are available from the corresponding author by request.

351

352 **Competing interests**

353 The authors declare that they have no competing interests.

354

355 **References**

356 1. Yehia S, Tuan CY Bridge deck deicing. In: Transportation Conference Proceedings, Iowa State University, Ames,
357 1998. pp 51-57.

358 2. Fischel M (2001) Evaluation of selected deicers based on a review of the literature CDOT-DTD-R-2001-15.
359 Colorado Department of Transportation, Denver.

360 3. Mussato BT, Gepreags OK, Farnden G (2004) Relative effects of sodium chloride and magnesium chloride on
361 reinforced concrete: State of the art. Transportation Research Record 1866 (1):59-66.

362 doi:<https://doi.org/10.3141/1866-08>

363 4. Ramakrishna DM, Viraraghavan T (2005) Environmental Impact of Chemical Deicers – A Review. Water, Air,
364 and Soil Pollution 166 (1):49-63. doi:<https://doi.org/10.1007/s11270-005-8265-9>

365 5. Ababneh A, Benboudjema F, Xi YP (2003) Chloride penetration in nonsaturated concrete. Journal of Materials in
366 Civil Engineering 15 (2):183-191. doi:[https://doi.org/10.1061/\(Asce\)0899-1561\(2003\)15:2\(183\)](https://doi.org/10.1061/(Asce)0899-1561(2003)15:2(183))

367 6. Bastidas-Arteaga E, Chateauneuf A, S A Nchez-Silva M, Bressolette P, Schoefs F (2011) A comprehensive
368 probabilistic model of chloride ingress in unsaturated concrete. Eng Struct 33 (3):720-730.

369 doi:<https://doi.org/10.1016/j.engstruct.2010.11.008>

370 7. Qiao C, Suraneni P, Tsui Chang M, Weiss J (2018) Damage in cement pastes exposed to MgCl₂ solutions.

371 Materials and Structures 51 (3):74. doi:<https://doi.org/10.1617/s11527-018-1191-2>

- 372 8. Qiao C, Suraneni P, Weiss J (2018) Flexural strength reduction of cement pastes exposed to CaCl₂ solutions.
373 Cement and Concrete Composites 86:297-305. doi:<https://doi.org/10.1016/j.cemconcomp.2017.11.021>
- 374 9. Sutter L, Peterson K, Touton S, Van Dam T, Johnston D (2006) Petrographic evidence of calcium oxychloride
375 formation in mortars exposed to magnesium chloride solution. Cement and Concrete Research 36 (8):1533-1541.
376 doi:<http://dx.doi.org/10.1016/j.cemconres.2006.05.022>
- 377 10. Farnam Y, Wiese A, Bentz D, Davis J, Weiss J (2015) Damage development in cementitious materials exposed
378 to magnesium chloride deicing salt. Construction and Building Materials 93:384-392.
379 doi:<http://dx.doi.org/10.1016/j.conbuildmat.2015.06.004>
- 380 11. Qiao C, Ni W, Wang Q, Weiss J (2018) Chloride Diffusion and Wicking in Concrete Exposed to NaCl and
381 MgCl₂ Solutions. Journal of Materials in Civil Engineering 30 (3):04018015.
382 doi:[http://dx.doi.org/10.1061/\(ASCE\)MT.1943-5533.0002192](http://dx.doi.org/10.1061/(ASCE)MT.1943-5533.0002192)
- 383 12. Chatterji S (1978) Mechanism of the CaCl₂ attack on Portland cement concrete. Cement and Concrete Research
384 8 (4):461-467. doi:[http://dx.doi.org/10.1016/0008-8846\(78\)90026-1](http://dx.doi.org/10.1016/0008-8846(78)90026-1)
- 385 13. Smith SH, Qiao C, Suraneni P, Kurtis KE, Weiss WJ (2019) Service-life of concrete in freeze-thaw
386 environments: Critical degree of saturation and calcium oxychloride formation. Cement and Concrete Research
387 122:93-106. doi:<https://doi.org/10.1016/j.cemconres.2019.04.014>
- 388 14. Jones C, Ramanathan S, Suraneni P, Hale WM (2020) Calcium oxychloride: A critical review of the literature
389 surrounding the formation, deterioration, testing procedures, and recommended mitigation techniques. Cement and
390 Concrete Composites 113:103663. doi:<https://doi.org/10.1016/j.cemconcomp.2020.103663>
- 391 15. Peterson K, Julio-Betancourt G, Sutter L, Hooton RD, Johnston D (2013) Observations of chloride ingress and
392 calcium oxychloride formation in laboratory concrete and mortar at 5° C. Cement and Concrete Research 45:79-90.
393 doi:<https://doi.org/10.1016/j.cemconres.2013.01.001>
- 394 16. Collepardi M, Coppola L, Pistolesi C Durability of concrete structures exposed to CaCl₂ based deicing salts. In:
395 Proceedings of the 3rd CANMENT/ACI International Conference, France, 1994. American Concrete Institute,
396 Farmington Hills, MI, pp 107-120
- 397 17. Hornain H, Marchand J, Ammouche A, Commène JP, Moranville M (1996) Microscopic observation of cracks
398 in concrete — A new sample preparation technique using dye impregnation. Cement and Concrete Research 26
399 (4):573-583. doi:[https://doi.org/10.1016/0008-8846\(96\)00032-4](https://doi.org/10.1016/0008-8846(96)00032-4)
- 400 18. Ammouche A, Breyse D, Hornain H, Didry O, Marchand J (2000) A new image analysis technique for the
401 quantitative assessment of microcracks in cement-based materials. Cement and Concrete Research 30 (1):25-35.
402 doi:[https://doi.org/10.1016/S0008-8846\(99\)00212-4](https://doi.org/10.1016/S0008-8846(99)00212-4)
- 403 19. Litorowicz A (2006) Identification and quantification of cracks in concrete by optical fluorescent microscopy.
404 Cement and Concrete Research 36 (8):1508-1515. doi:<https://doi.org/10.1016/j.cemconres.2006.05.011>
- 405 20. Zhou C, Li K, Pang X (2012) Geometry of crack network and its impact on transport properties of concrete.
406 Cement and Concrete Research 42 (9):1261-1272. doi:<https://doi.org/10.1016/j.cemconres.2012.05.017>
- 407 21. Schindelin J, Arganda-Carreras I, Frise E, Kaynig V, Longair M, Pietzsch T, Preibisch S, Rueden C, Saalfeld S,
408 Schmid B, Tinevez J-Y, White DJ, Hartenstein V, Eliceiri K, Tomancak P, Cardona A (2012) Fiji: an open-source
409 platform for biological-image analysis. Nature Methods 9 (7):676-682. doi:10.1038/nmeth.2019
- 410 22. Walker HN, Lane DS, Stutzman PE (2006) Petrographic Methods of Examining Hardened Concrete: A
411 Petrographic Manual. Federal Highway Administration, McLean, VA

- 412 23. Wong HS, Poole AB, Wells B, Eden M, Barnes R, Ferrari J, Fox R, Yio MHN, Copuroglu O, Guðmundsson G,
413 Hardie R, Jakobsen UH, Makoubi K, Mitchinson A, Raybould P, Strongman J, Buenfeld NR (2020) Microscopy
414 techniques for determining water–cement (w/c) ratio in hardened concrete: a round-robin assessment. *Materials and*
415 *Structures* 53 (2):25. doi:<https://doi.org/10.1617/s11527-020-1458-2>
- 416 24. Qiao C, Rothstein D (2020) Microstructural Evaluation of Durability of Different Cementitious Mixtures in
417 Microbial Induced Corrosion Environments. Paper presented at the XV International Conference on Durability of
418 Building Materials and Components, Barcelona, Spain, October, 20-23, 2020
- 419 25. Katayama T, Tagami M, Sarai Y, Izumi S, Hira T (2004) Alkali-aggregate reaction under the influence of
420 deicing salts in the Hokuriku district, Japan. *Materials Characterization* 53 (2):105-122.
421 doi:<https://doi.org/10.1016/j.matchar.2004.07.003>
- 422 26. Rothstein D, Qiao C (2020) Accelerated Expansion Test Sample Report: DRP. In: Saouma VE (ed) *Diagnosis &*
423 *Prognosis of AAR Affected Structures: State-of-the-Art Report of the RILEM Technical Committee 259-ISR.*
424 *RILEM State-of-the-Art Reports*, vol 31, 1 edn. RILEM, p 594. doi:https://doi.org/10.1007/978-3-030-44014-5_16
- 425 27. ASTM C856 / C856M-20, Standard Practice for Petrographic Examination of Hardened Concrete (2020). ASTM
426 International, West Conshohocken, PA. doi:https://doi.org/10.1520/C0856_C0856M-20
- 427 28. Steger C (1998) An unbiased detector of curvilinear structures. *IEEE Transactions on Pattern Analysis and*
428 *Machine Intelligence* 20 (2):113-125. doi:<https://doi.org/10.1109/34.659930>
- 429 29. Qiao C, Suraneni P, Weiss J (2018) Phase diagram and volume change of the Ca(OH)₂-CaCl₂-H₂O system for
430 varying Ca(OH)₂/CaCl₂ molar ratios. *Journal of Materials in Civil Engineering* 30 (2):04017281.
431 doi:[https://doi.org/10.1061/\(ASCE\)MT.1943-5533.0002145](https://doi.org/10.1061/(ASCE)MT.1943-5533.0002145)
- 432 30. Suryavanshi AK, Scantlebury JD, Lyon SB (1996) Mechanism of Friedel's salt formation in cements rich in tri-
433 calcium aluminate. *Cement and Concrete Research* 26 (5):717-727. doi:[https://doi.org/10.1016/s0008-](https://doi.org/10.1016/s0008-8846(96)85009-5)
434 [8846\(96\)85009-5](https://doi.org/10.1016/s0008-8846(96)85009-5)
- 435 31. Birnin-Yauri UA, Glasser FP (1998) Friedel's salt, Ca₂Al(OH)₆(Cl,OH)·2H₂O: Its solid solutions and their role
436 in chloride binding. *Cement and Concrete Research* 28 (12):1713-1723. doi:[http://dx.doi.org/10.1016/S0008-](http://dx.doi.org/10.1016/S0008-8846(98)00162-8)
437 [8846\(98\)00162-8](http://dx.doi.org/10.1016/S0008-8846(98)00162-8)
- 438 32. Qiao C, Suraneni P, Then NWY, Choudhary A, Weiss J (2019) Chloride binding of cement pastes with fly ash
439 exposed to CaCl₂ solutions at 5 and 23 °C. *Cement and Concrete Composites* 97:43-53.
440 doi:<https://doi.org/10.1016/j.cemconcomp.2018.12.011>
- 441 33. Famy C, Scrivener KL, Atkinson A, Brough AR (2001) Influence of the storage conditions on the dimensional
442 changes of heat-cured mortars. *Cement and Concrete Research* 31 (5):795-803. doi:[https://doi.org/10.1016/S0008-](https://doi.org/10.1016/S0008-8846(01)00480-X)
443 [8846\(01\)00480-X](https://doi.org/10.1016/S0008-8846(01)00480-X)
- 444 34. Galan I, Perron L, Glasser FP (2015) Impact of chloride-rich environments on cement paste mineralogy. *Cement*
445 *and Concrete Research* 68:174-183. doi:<http://dx.doi.org/10.1016/j.cemconres.2014.10.017>
- 446 35. Arganda-Carreras I, Kaynig V, Rueden C, Eliceiri KW, Schindelin J, Cardona A, Sebastian Seung H (2017)
447 Trainable Weka Segmentation: a machine learning tool for microscopy pixel classification. *Bioinformatics* 33
448 (15):2424-2426. doi:<https://doi.org/10.1093/bioinformatics/btx180>
- 449 36. Liao W, Sun X, Kumar A, Sun H, Ma H (2019) Hydration of Binary Portland Cement Blends Containing Silica
450 Fume: A Decoupling Method to Estimate Degrees of Hydration and Pozzolanic Reaction. *Frontiers in Materials* 6
451 (78). doi:<https://doi.org/10.3389/fmats.2019.00078>
- 452

Figures

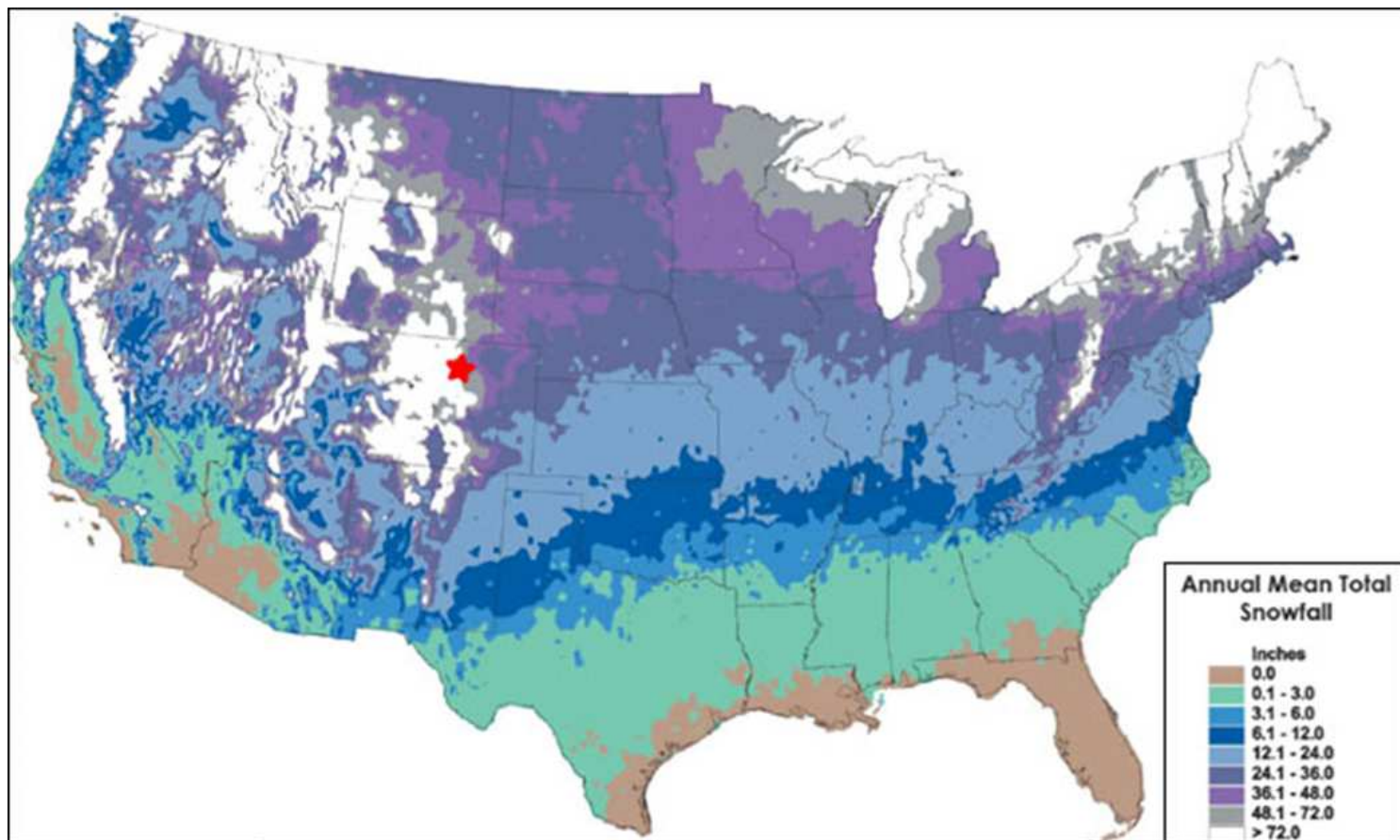


Figure 1

Average annual snowfall map of the contiguous US from US National Oceanic and Atmospheric Administration (<https://www.noaa.gov>). The red star indicates the location of the field samples. Note: The designations employed and the presentation of the material on this map do not imply the expression of any opinion whatsoever on the part of Research Square concerning the legal status of any country, territory, city or area or of its authorities, or concerning the delimitation of its frontiers or boundaries. This map has been provided by the authors.

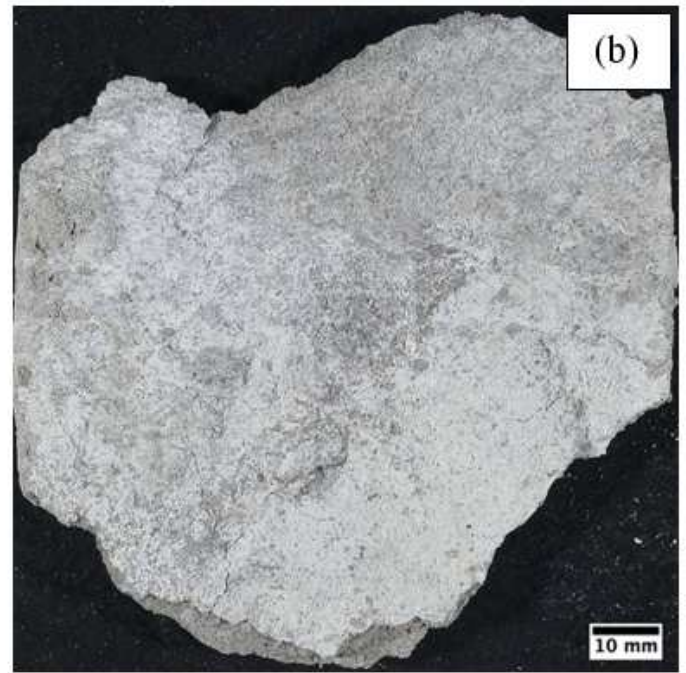
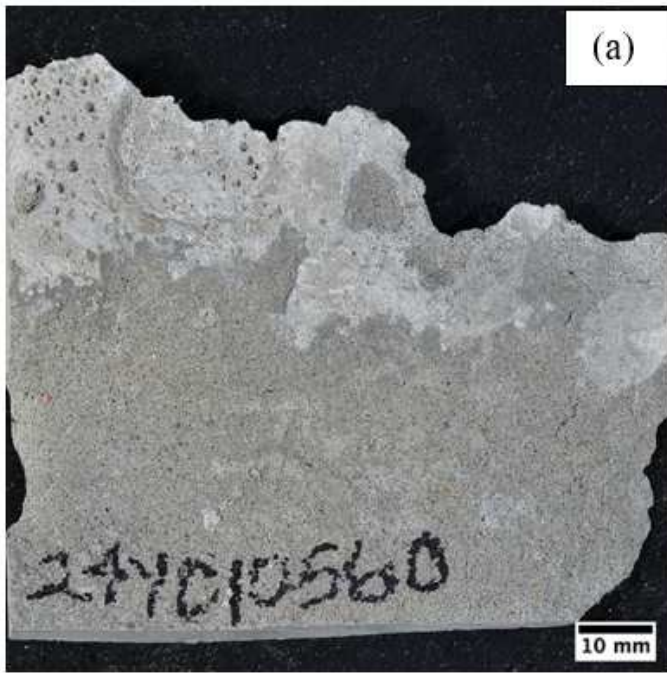


Figure 2

The conditions of the as-received fragments of the undamaged field mortar (a) and the damaged field mortar (b), respectively.

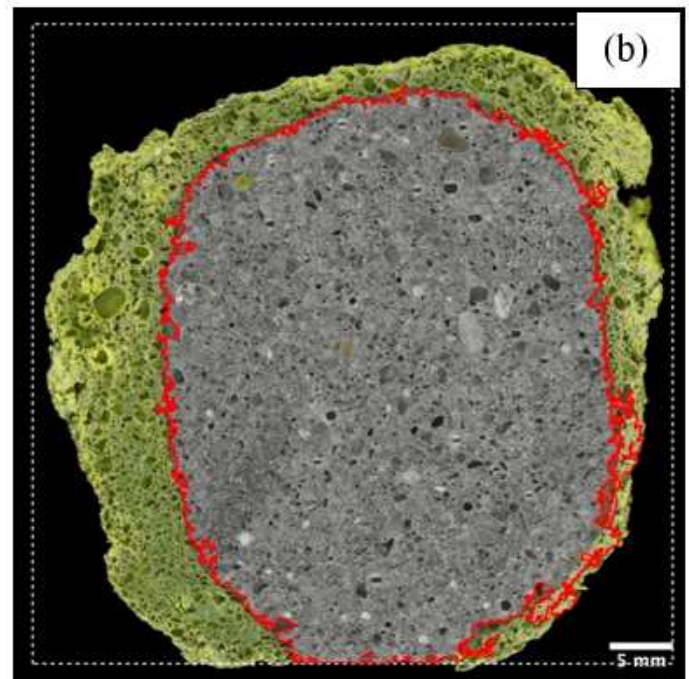
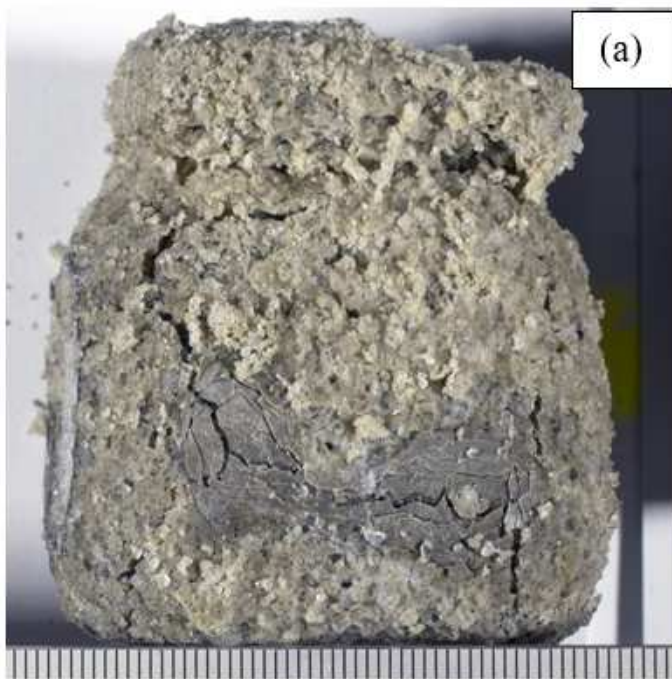


Figure 3

(a) Photograph showing condition of the lab-cast mortar after 51 freeze-thaw cycles under the submersion of a 25 wt. % CaCl_2 solution. Scale in millimeters. (b) Reflected light photomicrograph of the polished surface of the lab-cast mortar. White square and red curve indicate the original size and the

remaining intact zone of the sample, respectively. The yellow green color in (b) indicates the epoxied damage zone.

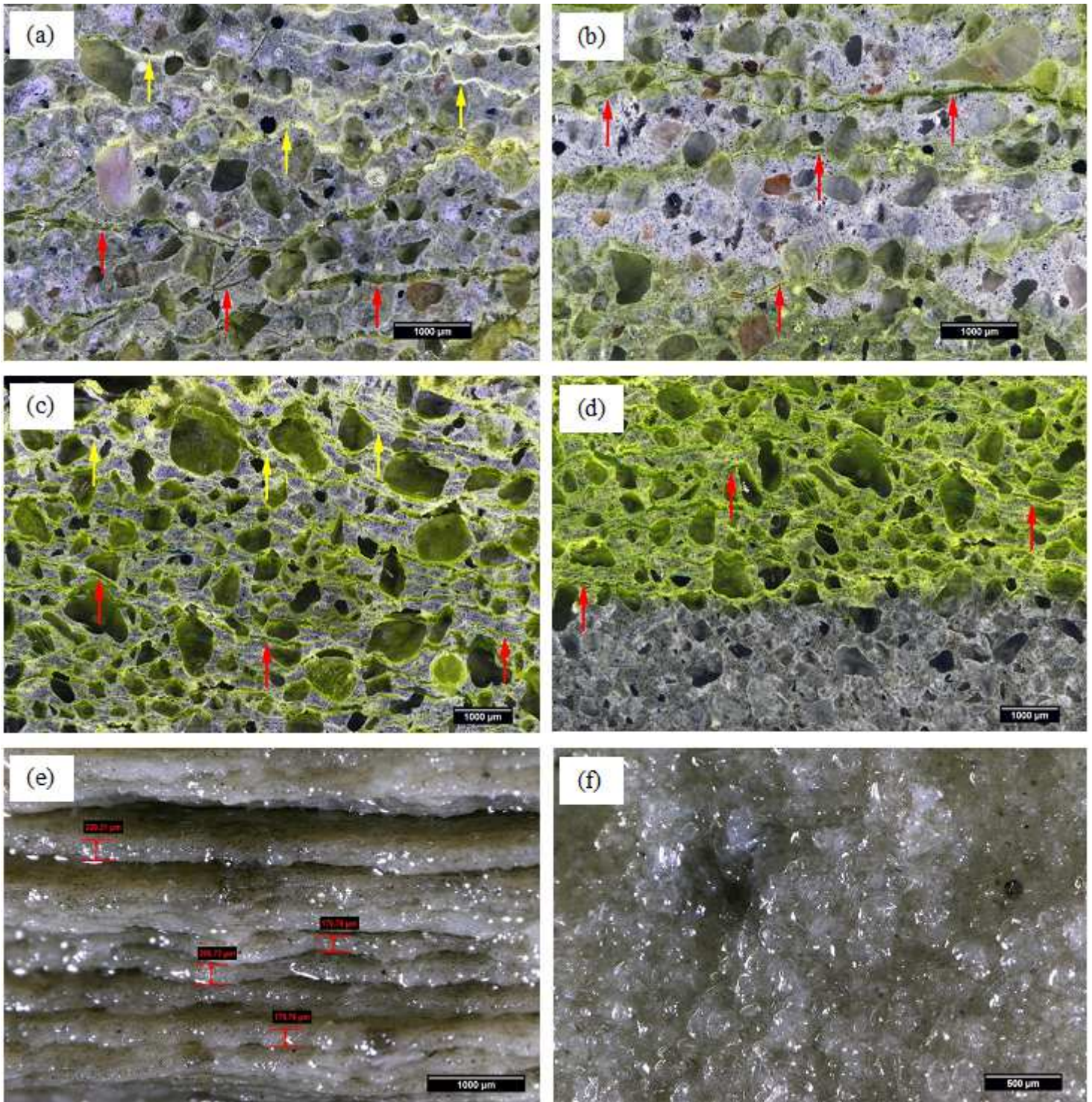


Figure 4

(a)-(d) Reflected light photomicrographs (RLP) of the polished surface of the damaged field mortar (a-b) and lab-cast mortar (c-d) showing horizontal cracks/microcracks at two different depths from the exposure surface, respectively. Zones in (a) and (c) are closer to the exposure surface. Yellow and red arrows indicate cracks/microcracks with and without secondary deposits, respectively. (e) Fresh

delamination sheets in the damaged lab-cast paste. (f) Transparent secondary deposits on the surface of the delamination sheet in (e).

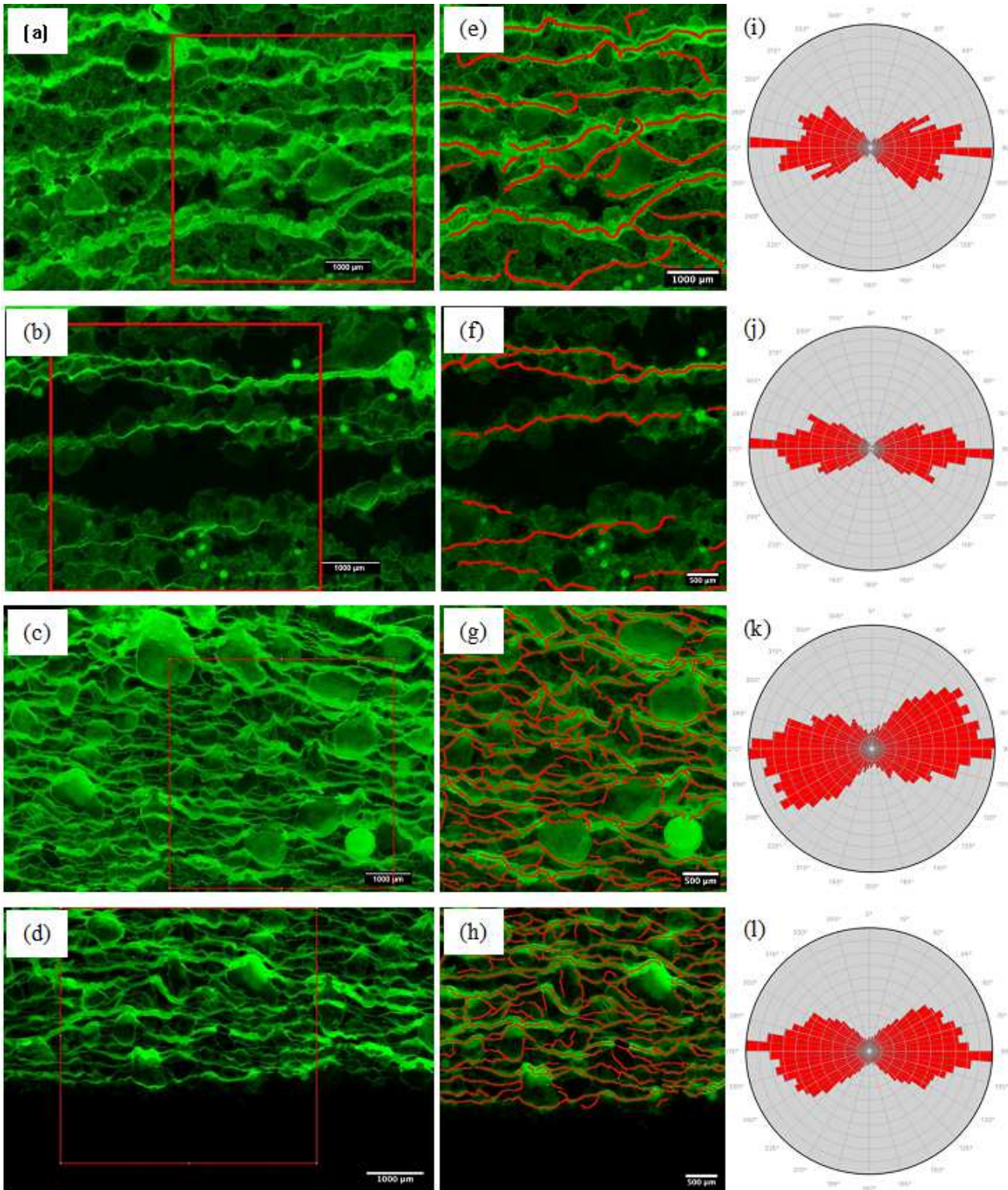


Figure 5

(a)-(b) Fluorescent reflected light photomicrographs (FRLP) of the polished surface of the damaged field mortar showing cracks/microcracks in the upper and lower zones from the top surface, respectively. (c)-(d) FRLP of the polished surface of the lab-cast mortar showing cracks/microcracks in the closer

(outward) and further (inward) zones from the outer surface, respectively. (e)-(h) Identified crack network in the red zone in (a)-(d). (i)-(l) Rose diagrams showing the cracking orientation in (e)-(h).

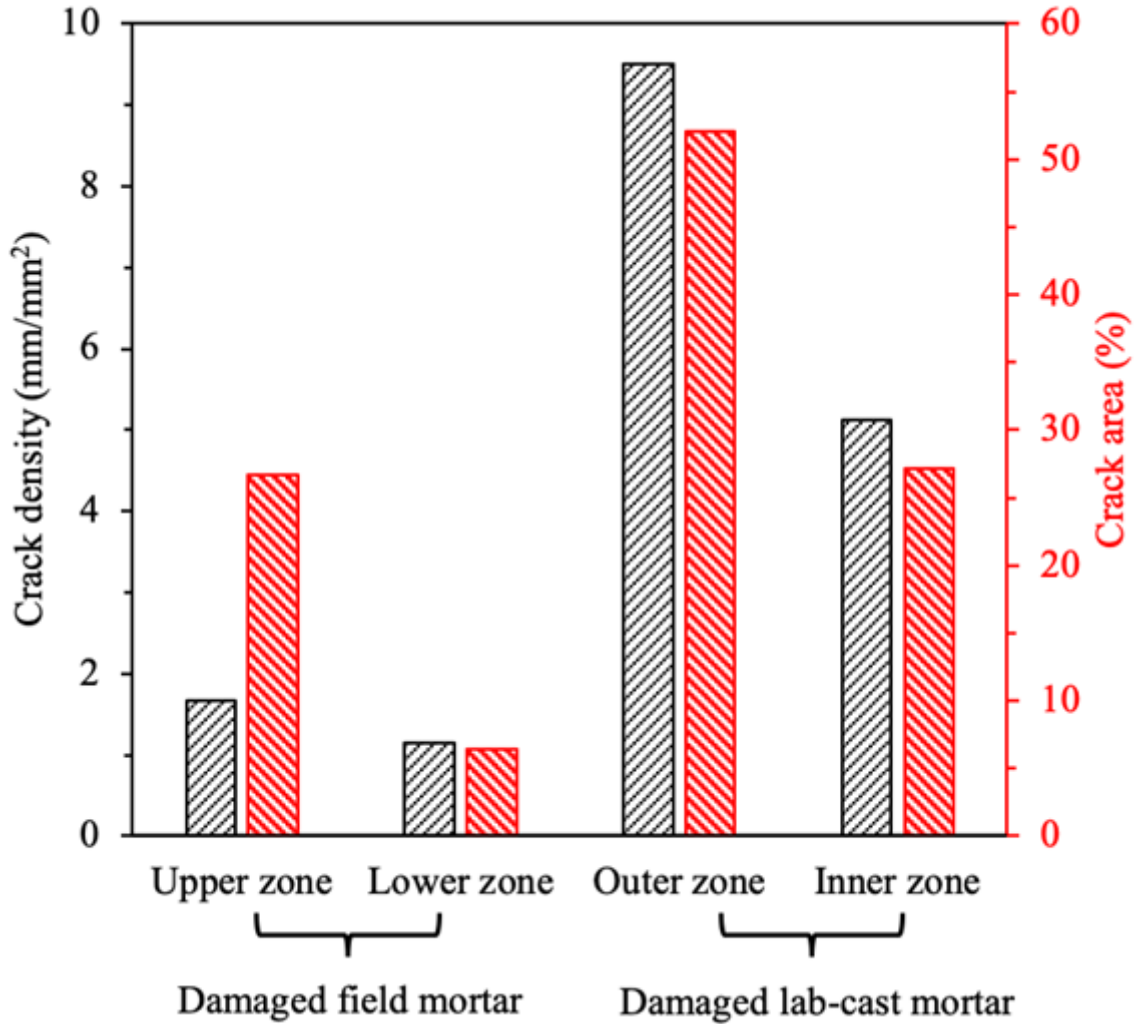


Figure 6

Crack density (left series) and crack area fraction (right series) in different zones of the field damaged field mortar and lab-cast mortar.

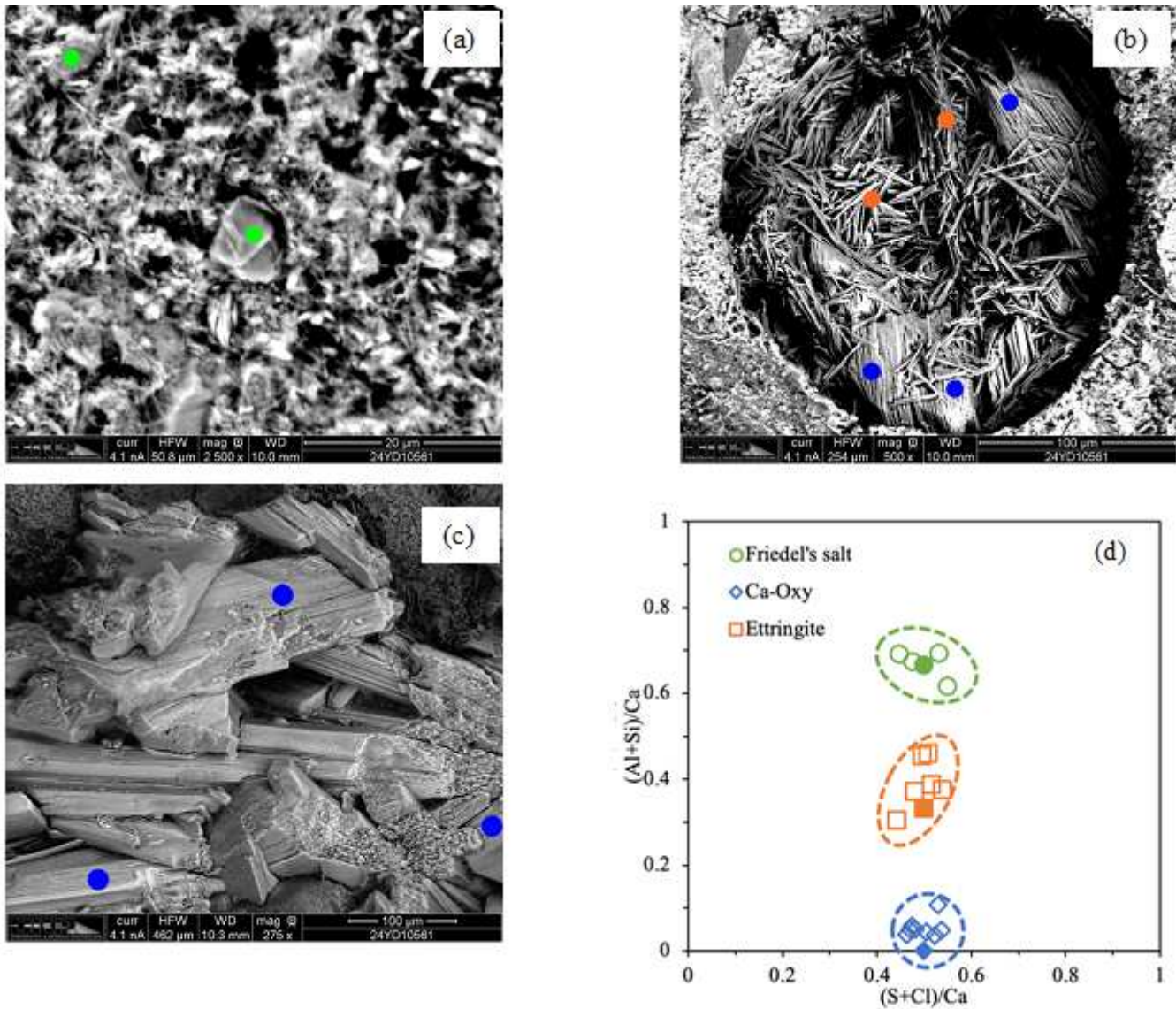


Figure 7

(a)-(c) Backscattered electron (BSE) images of secondary deposits in (a) the paste matrix, (b) an entrained air void and (c) a fresh fracture surface, respectively. Green circles: Friedel's salt, blue diamonds: Ca-Oxy; orange squares: ettringite. (d) Atomic ratios obtained from EDX spectra in zones in (a)-(c). The solid shapes indicate the theoretical composition of the corresponding minerals.

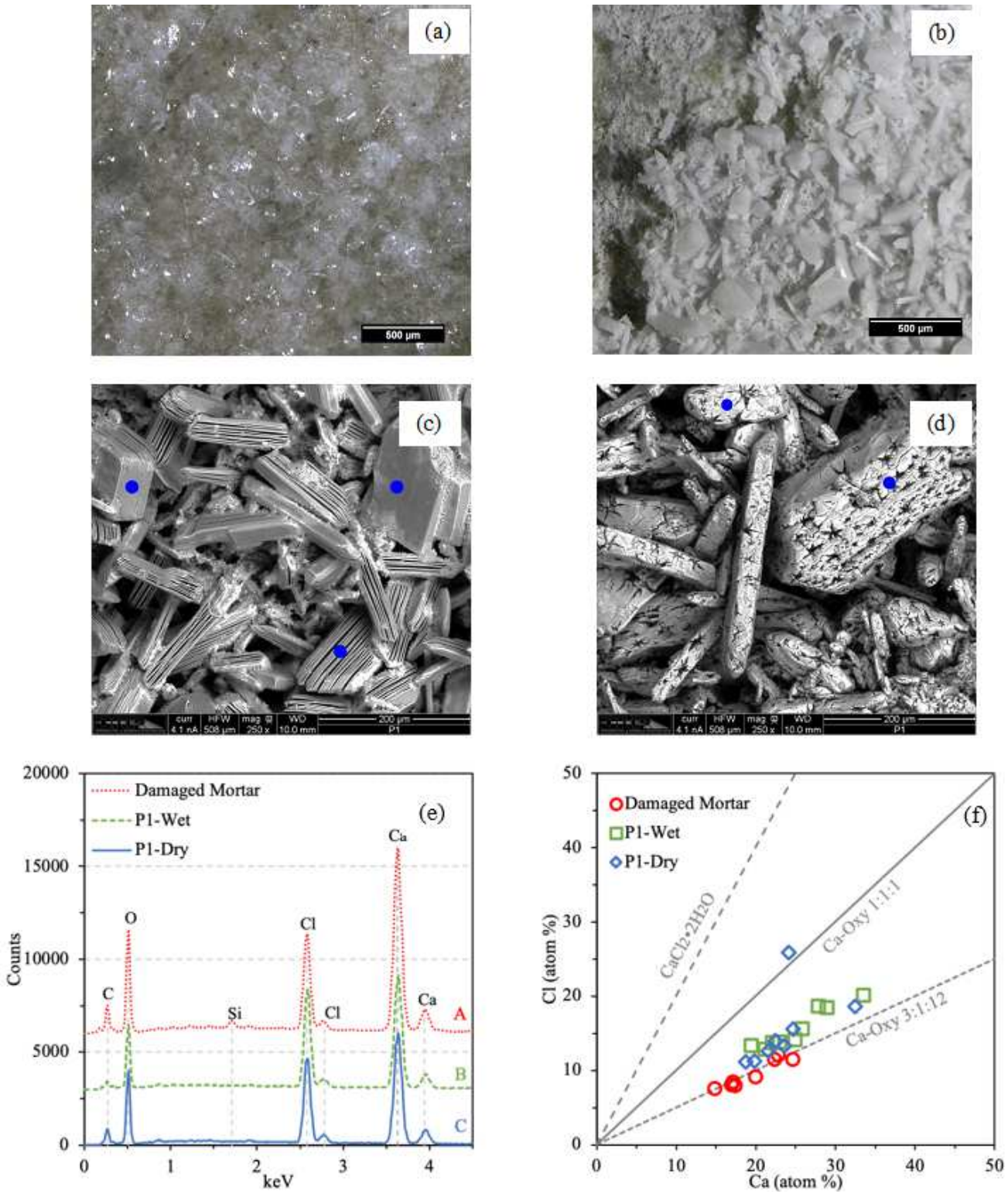


Figure 8

(a)-(b) RLP and (c)-(d) BSE images of Ca-Oxy (blue solid dots) in (a)/(c) an originally wet condition and (b)/(d) a dried condition on a fracture surface of OPC paste, respectively. (e) EDX spectra obtained from zones in Fig. 5c and Fig. 6a-6b. (f) Relationship between Ca and Cl contents of Ca-Oxy observed from EDX overlaid with theoretical Ca-Oxy formulae.

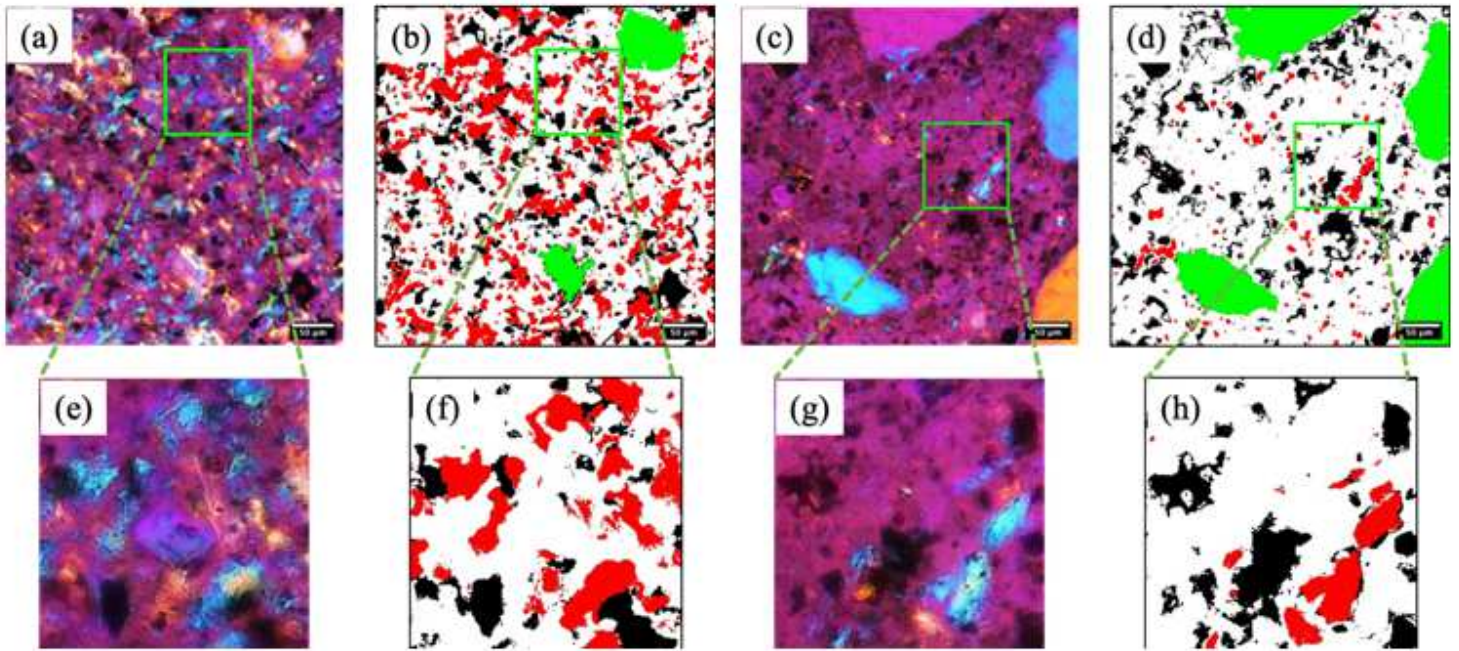


Figure 9

(a)&(c) Transmitted light photomicrographs showing paste in the middle of the (a) undamaged field mortar and (c) damaged field mortar, respectively, in cross-polarized light with the gypsum first order retardation plate inserted. (b)&(d) Segmentation images of the photomicrographs in (a) and (c) using 2D Trainable Weka Segmentation in ImageJ [35]. (e)-(h) Zoomed-in images of the corresponding zones in (a)-(d). The size of the zone in (e)-(h) is 100 μm by 100 μm .

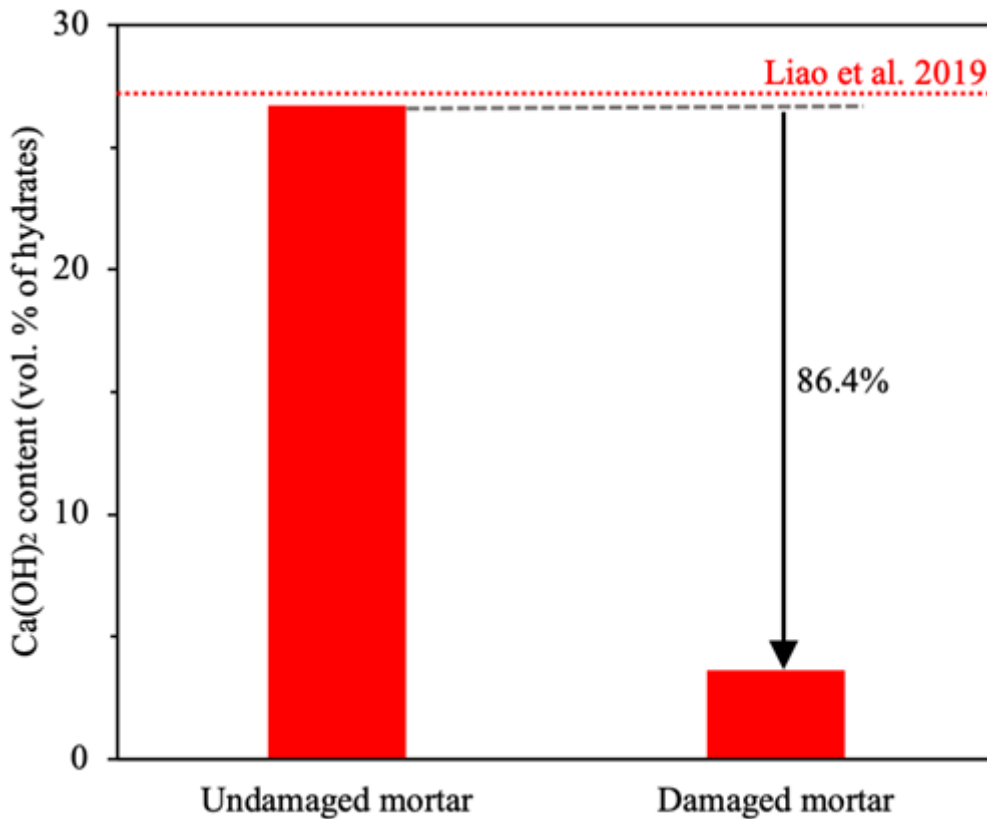


Figure 10

Quantification of $\text{Ca}(\text{OH})_2$ contents in the mortars using image analysis. The red dotted line indicates the value from Ref. [36].